High spatial and temporal resolution sampling of Martian gas abundances from CRISM spectra

Anthony D. Toigo,[1] Michael D. Smith,[2] Frank P. Seelos,[1] and Scott L. Murchie[1]

[1] The Compact Reconnaissance Imaging Spectrometer for Mars on the Mars Reconnaissance Orbiter spacecraft has been collecting spectra in the visible to near-infrared wavelength range for over 5 years (approximately 3 Martian years). Observations consist of image cubes, with two main selections of spectral sampling (74 and 545 spectral channels) and two main selections of spatial sampling (approximately 20 and 200 m/pixel). Retrievals of gas abundances, specifically CO_2, H_2O, and CO, are performed from spectra collected in all observation modes. The retrievals are efficiently performed using a look-up table, where the strength of gas absorption features are precalculated for an N-dimensional discrete grid of known input parameters (season, location, environment, viewing geometry, etc.) and the one unknown parameter to be retrieved (gas abundance). A reverse interpolation in the look-up table is used to match the observed strength of the gas absorption to the gas abundance. This algorithm is extremely fast compared to traditional radiative transfer computations that seek to recursively fit calculated results to an observed spectral feature, and can therefore be applied on a pixel-by-pixel basis to the tens of thousands of Compact Reconnaissance Imaging Spectrometer for Mars images, to examine cross-scene structure as well as to produce climatological averages.

1. Introduction

[2] The Compact Reconnaissance Imaging Spectrometer for Mars (CRISM) on the Mars Reconnaissance Orbiter (MRO) spacecraft has been collecting spectra in the visible to near-infrared wavelength range for over 5 years (approximately 3 Martian years). One of the primary objectives for the instrument is atmospheric monitoring to characterize the spatial and temporal properties of the atmosphere for studies of the climate, weather, and photochemistry [*Murchie et al.*, 2007]. In pursuit of that objective, mapping of the atmospheric dust and various gas species in the atmosphere has been carried out [*Wolff et al.*, 2009; *Smith et al.*, 2009; *Clancy et al.*, 2012; *Smith et al.*, 2012].

[3] A precursor work, *Smith et al.* [2009], performed retrievals of the abundances of the gases CO_2, CO, and H_2O using averaged spectra from a central subregion of gimballed, hyperspectral observations by CRISM. These retrievals were performed by doing a detailed, iterative radiative transfer calculation on spectra in the highest spectral resolution mode. That process, although accurate, suffers a disadvantage of slow speed, because each individual radiative transfer calculation can take much time, several calculations are necessary for each spectrum, and these must be repeated for tens of thousands of pixels in each of the tens of thousands of observations available over the entire mission (about 8 billion total spectra).

[4] This work extends that precursor work in two ways. One, the retrieval process has been extended to include the lower spectral resolution multispectral observations. Two, a look-up table (LUT) method is employed to increase the speed with which the retrievals can be performed with only a small loss in accuracy compared to the radiative transfer (RT) method of the precursor works.

[5] In this paper, we present the results of these gas abundance retrievals for all types of CRISM observations using the LUT method from over the more than 5 years of operation. Details of the CRISM instrument, observation modes, and the spectral data are discussed in section 2. Section 3 discusses the retrieval algorithm. Section 4 presents and discusses the results of the retrievals.

2. Mission, Instrument, and Data

2.1. Mars Reconnaissance Orbiter Mission

[6] MRO has been making regular observations of Mars with its various instruments since the beginning of its primary mission in November 2006. The spacecraft is in a Sun-synchronous, near-polar orbit (about 3° inclination) of Mars at an altitude of approximately 300 km. The local time

---

[1]The Johns Hopkins University Applied Physics Laboratory, Laurel, Maryland, 20723, USA.
[2]NASA/GSFC, Greenbelt, Maryland, 20771, USA.

Corresponding author: A. D. Toigo, The Johns Hopkins University Applied Physics Laboratory, Laurel, MD 20723, USA. (Anthony.Toigo@jhuapl.edu)

for the dayside portions of the orbit is approximately 1500 LT [*Zurek and Smrekar*, 2007].

2.2. CRISM Instrument

[7] The CRISM [*Murchie et al.*, 2007, 2009] is a hyperspectral imager with a spatial resolution of 15–19 m/pixel collecting data in the visible and near-infrared wavelength regions (362 to 3920 nm) at a spectral sampling of about 6.55 nm/channel. Two detectors are available, each 640 (spatial) by 480 (spectral) pixels: the VNIR detector (362–1053 nm, using 107 active [i.e., nonmasked] channel pixels) and the IR detector (1002–3920 nm, using 438 active channel pixels). Observations can either utilize the instrument's gimbal to acquire longer integration time per pixel ("targeted observations"), or collect data in a nadir-pointing push-broom-like manner ("mapping observations"). Pixels can be binned 2×, 5×, or 10× in the spatial direction, with binning performed on board. No pixel binning in the spectral direction is available, but user-definable selections of spectral channels can be chosen for return. In full spectral resolution ("hyperspectral observations") all 545 spectral channels are returned. A 74-channel subset ("multispectral observations"), optimized for surface and atmospheric features, is also present. Intermediate modes with full spectral resolution in the visible (107 channels) with or without a 154-channel subset in the infrared are available, but are not used in the results presented in the this paper.

2.3. Observation Modes

[8] CRISM has three primary types of observation modes combining the spatial and spectral configurations just described.

[9] In multispectral mapping observation (MMO) mode, the instrument is pointed at planet nadir, data are collected at a frame rate of 15 Hz, the 74 wavelength channel subset is returned, and data is binned at a width of 10 pixels to a spatial resolution of approximately 200 m/pixel. Images are thus typically 64 pixels wide (cross-track), and the duration of observation acquisition is typically 15, 60, or 180 s, encompassing an along-track spatial pixel extent of up to 2700 pixels.

[10] In targeted hyperspectral observation (THO) mode, the instrument sensor is panned with a gimbal to remove most along-track motion, and a specific region of interest, approximately 10 km by 10 km, is mapped at full spatial and spectral resolution. In spatial dimensions, this is 640 pixels cross-track and approximately 400 to 500 pixels along-track, the exact number depending on the observation geometry. Up to 10 additional short, spatially binned (10×) images are taken before and after the main central image, providing the capability to calculate an emission phase function of the site for atmospheric study. For the purposes of the study here, these extra emission phase function sequences are ignored.

2.4. Spectra

[11] A typical CRISM multispectral observation spectrum is shown in Figure 1. Colored areas show the absorption feature regions that were used in this study. Abundances of three gases were retrieved in this study: CO_2, H_2O, and CO. CO_2, the main component of the atmosphere, is the strongest absorber and most readily retrieved. H_2O and CO are minor constituents whose absorption features are weaker and somewhat more difficult to retrieve. Other minor gas species (e.g., methane)
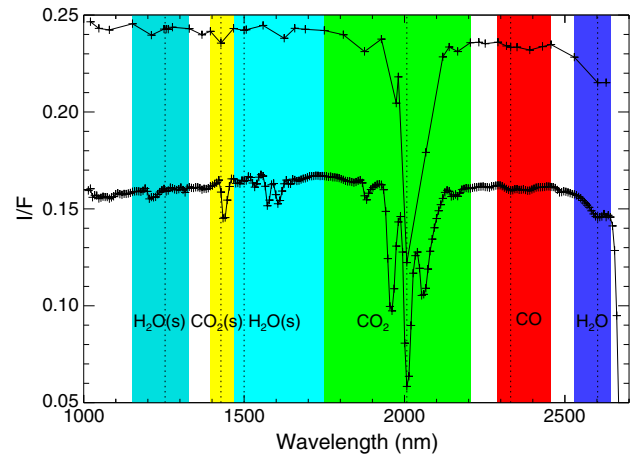
Figure 1. Sample hyperspectral (black) and multispectral (gray) observation spectra with absorption feature regions highlighted in color. The multispectral observation has been shifted upward by 0.05 to be seen clearly. The green, blue, and red areas show the spectral regions used for calculation of the absorption band depths of CO_2, H_2O, and CO, respectively. The cyan and yellow areas show the spectral regions used to test for the presence of H_2O and CO_2 ice, respectively. The dotted lines represent the absorption feature "center" for our purposes. Both spectra are averages over an approximately 2 km square area at the center of the observation. Hyperspectral observation: FRT0000901A; Multispectral observation: MSP00008574.

have absorption features that are too weak to be detected by CRISM.

[12] For each region, the absorption feature was defined by picking a "center" spectral channel closest to the peak of the absorption feature, and then two "continuum" channels at wavelengths surrounding the center. All three channels were picked from the multispectral subset, in order to ensure that retrieval calculations could be performed consistently for all types of observation modes. Table 1 lists the channels (and approximate wavelengths) used for each of the gas absorption features.

[13] Additionally, three extra absorption features outside the gas bands were also considered: CO_2 and H_2O ice. Two separate bands for H_2O ice were considered, each band being sensitive to different ice grain sizes. Since the presence of

Table 1. Wavelengths and (Hyperspectral) Channels Defining the Atmospheric Absorption Bands in the Retrieval Algorithm[a]

Species	Wavelength (nm) [channel]	
	Center	Continuum
CO_2 (g)	2007 [285]	1750 [324], 2205 [255]
H_2O (g)	2602 [195]	2530 [206], 2641 [189]
CO (g)	2331 [236]	2291 [242], 2457 [217]
CO_2 (s)	1428 [373]	1395 [378], 1467 [367]
H_2O (s)	1254 [399]	1152 [415], 1329 [388]
H_2O (s)	1500 [362]	1395 [378], 1750 [324]

[a]Wavelengths and (hyperspectral) channels used to define the absorption bands of the various species used in the retrieval process. (In the CRISM IR detector, channel numbers increase from long to short wavelengths.)

either ice could affect the retrieval of the gases, ice absorption feature strength was used as one determinant of the quality of a gas abundance retrieval (see section 3.4 below).

[14] One major motivation for this study was to take advantage of the vast number of CRISM MMOs available for climatological averages and for individual investigation. Figure 2 shows a number density map of the seasonal and latitudinal distribution of MMOs and THOs. Areas near the pole where observations are missing are either due to instrument observation restrictions (incidence angle of observation less than 75°, typically) or filtering out contamination from ground ice (see section 3.4 below). The vertical gaps are due to solar conjunction or spacecraft and instrument anomalies. The precursor paper, *Smith et al.* [2009], focused on analysis of the THOs using the iterative RT method. The quicker algorithm described here made possible the use of the greater number and extent of MMOs relative to THOs.

3. Retrieval Algorithm

[15] The precursor work, *Smith et al.* [2009], focused on retrievals of gas abundance from THOs using full, iterative radiative transfer calculations. Due to the complexity of those retrieval calculations, each individual retrieval takes an appreciable amount of time. In

particular, the time required for the retrievals makes it impractical to do a retrieval on the spectrum of each individual pixel in every THO. Instead, an average spectrum is defined for a subregion of the THO about 2 km square at the center of the observation. While the averaging has the advantages of increasing the speed of calculation and reducing the measurement noise, it does so at the expense of being able to observe within-scene variations (e.g., topographic variations, etc.; also see section 4.2). A related work on retrievals of gas abundance from CRISM observations, *Smith et al.* [2012], also uses the full, iterative radiative transfer calculations, but focuses on limb-geometry observations which are unique and entirely different from the nadir and near-nadir observations discussed here.

[16] Two major motivations for this work were to take advantage of the large number of MMOs also available, and also to attempt to perform retrievals on the spectrum of each individual pixel in either type of observation mode (THO and MMO). To achieve those goals, a LUT algorithm was chosen rather than a method consisting only of iterative full RT calculations. This was deemed to be an acceptable compromise between achieving the speed necessary to perform the orders of magnitude more retrievals in a reasonable time, while only introducing a minimal amount of error relative to the more accurate RT method. A similar
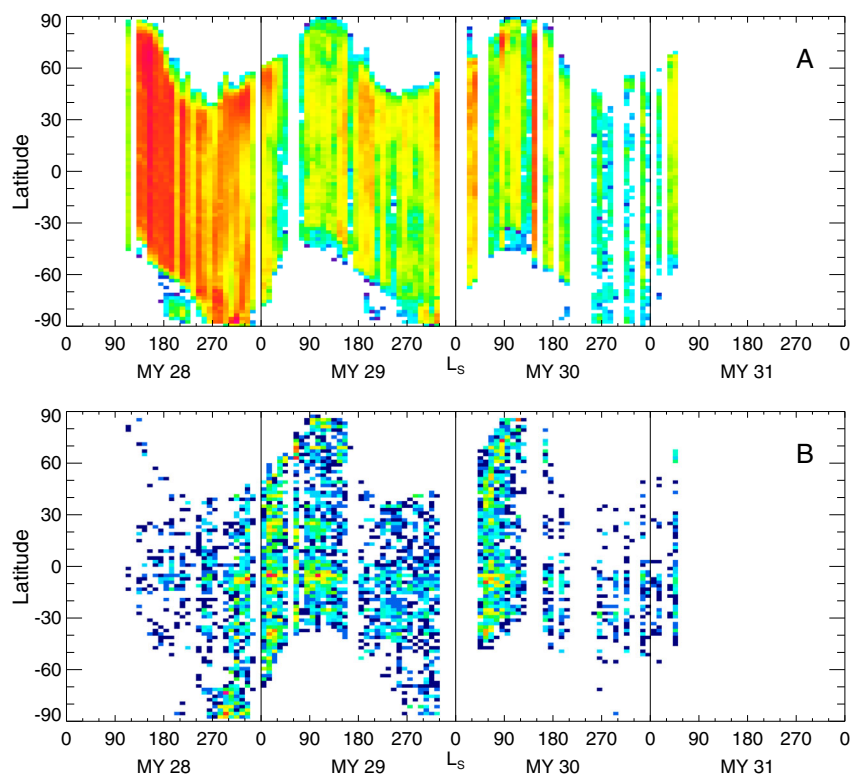
Figure 2. Number density of CRISM (A) MMO and (B) THO observations by latitude and season over the MRO mission. Scaling is arbitrary, but monotonic; red is many, blue is few, and white is none. Scaling is also not the same for the two different observation types. Early in the MRO mission, a dedicated mapping campaign led to the high density of MMO observations seen in the first year. Gaps due to the polar night can also be seen. Vertical bands of missing observations are due to solar conjunction, spacecraft anomalies, or instrument anomalies.

look-up table algorithm procedure has been used previously to retrieve surface pressure from Mars Express/OMEGA observations [*Forget et al.*, 2007]. In this section, we describe the LUT retrieval algorithm used in this work.

3.1. Look-Up Table

[17] The LUT algorithm is in essence a very large, multidimensional interpolation framework. The speed of this approach versus the RT method comes from the fact that the calculation of the LUT, while slow in and of itself, needs only be done once, and then all further retrievals in observations are done by fast, efficient, straightforward multidimensional interpolations.

[18] The LUT is also an n-dimensional "hypercube" rather than a strictly two-dimensional table. The n dimensions correspond to the n different parameters that are the necessary independent variable inputs into the RT code. These parameters then form the axes of the hypercube. However, the axes are discrete, as only m values of the parameter are chosen and used when performing the RT band depth calculations. This discretization of parameter values helps keep the number of calculations within reasonable limits and time to perform. Thus, there are m^n cells in the table.

[19] In practice, the number of discrete values per parameter, m, is not a constant, and the number of values, as well as the exact value chosen, is dependent on the actual parameter, i.e., $m \rightarrow m_i$. The number of discrete values per parameter is generally, however, of similar magnitude to all of the others, and thus the number of cells in the table, $\prod_{i=1}^{n} m_i$, is of order m^n. The relative sensitivity of the results to the input parameters guides the number of values chosen, while the environmental and geometric conditions experienced by Mars and the MRO spacecraft determine the range of values chosen. The exact list of parameters and values used is shown in Table 2.

[20] The first three parameters in Table 2 are geometric, and depend on the orientation of the MRO spacecraft and the Sun at the time the observation is made. The next four are atmospheric environmental parameters. The final four parameters are the retrieval quantities of interest. More values were chosen spanning the range of observed or expected values where accuracy was wanted (gas abundance parameters) or where ranges were large (geometric

parameters), while fewer values were chosen in the less sensitive atmospheric environmental parameters. The values at the extremes of any given parameter were not always physically achieved but serve to ensure that any quantity encountered in the observational data is an interpolation (rather than an extrapolation outside the LUT).

[21] There are also, in practice, six LUTs: one for gas absorption band continuum albedo and one for gas absorption band strength, for each of the three gases. The gas absorption band continuum albedo is not dependent on either the atmospheric environment or the gas abundance, and the albedo LUT in actuality has only five dimension parameters: solar incidence angle (μ_0), emission angle (μ), phase angle (φ), optical depth (τ), and albedo (A). Additionally, the number of parameters in the three gas abundance LUTs is not uniformly 9 (3 geometric, 4 environmental, 1 albedo, and 1 gas abundance) since surface pressure is actually a necessary input for the radiative transfer calculation (in an absorption band). Because CO_2 is the primary component of the Martian atmosphere, retrieval of CO_2 is essentially a determination of the surface pressure. The other two gas abundance LUTs then have 10 parameter dimensions: 3 geometric, 4 environmental, 1 albedo, 1 surface pressure, and then 1 gas abundance (either H_2O or CO).

[22] The values in the LUT cells are different, depending on the LUT type. For the albedo LUTs, the values in the cells are spectral continuum values, $R_{continuum}$, while the values in the cells of the gas abundance LUTs are absorption band depth strength, S. S was calculated by the following formula,

$$S = 1 - \frac{R_{center}}{R_{continuum}}, \quad (1)$$

and thus band strength index is a number between 0 and 1. In either case R refers to the measured radiation at the indicated wavelength. CRISM data in the Planetary Data System archive is stored in both radiance and I/F values. For this study, the I/F data were used for S above. R_{center} is the I/F value recorded in the absorption band center channel listed in Table 1. $R_{continuum}$ is the interpolated value of the continuum in the absence of any gas absorption. It is calculated by a simple linear interpolation of the two identified continuum channel values to the wavelength of the center channel.

Table 2. Input Parameters for the Look-up Table

Parameter	Symbol	Units	Values
Incidence angle (cosine)	μ_0		0.1, 0.3, 0.55, 0.75, 0.9
Emission angle (cosine)	μ		0.25, 0.5, 0.8, 0.9, 1
Phase angle (cosine)	φ		0.1, 0.35, 0.6, 0.85
Optical depth	τ		0.01, 0.1, 0.3, 0.5, 3
Near-surface air temperature	T_l	K	140, 180, 220, 270
Air temperature	T_h	K	140, 170, 200, 235
Surface temperature	T_s	K	140, 310
Albedo[a]	A		0, 0.1, 0.2, 0.3, 0.4, 0.5, 0.6, 0.7, 0.8, 0.9, 1.0
Surface pressure (CO_2)	P_s	mbar	1, 4, 5, 6, 7, 8, 9, 14
H_2O column vapor	h	precipitable microns	0, 5, 10, 15, 20, 30, 100
CO mixing ratio	X_{CO}	ppm	0, 300, 500, 700, 900, 1200, 2000

Input parameters used in the radiative transfer calculations to generate the look-up table.
[a]A subset of these values (0, 0.1, 0.2, 0.4, 0.6, 1) were used in the abundance look-up tables only.

3.2. Radiative Transfer Code

[23] The RT code used to calculate values in all LUT cells is described in more detail in *Smith et al.* [2009] and *Smith et al.* [2012]. The code calculates radiance as a function of wavelength based on various input parameters. The radiance can be (and are in this study) converted to an *I/F* value through normalization to an additional solar flux calculation.

[24] The values of the input parameters used to build all the LUTs are listed in Table 2. The continuum I/F quantities returned by the RT code are inserted directly into the cells of the albedo LUTs, while band strength indices are calculated from the RT code results and inserted into the gas abundance LUTs.

[25] Gas abundances input parameters are handled in different quantifications. Surface pressure is a necessary input and CO_2 abundance amount is treated as a constant fraction of surface pressure (0.9532, *Owen et al.* [1977]). Water vapor amounts are input as precipitable microns, i.e., the thickness of a surface layer of liquid if all of the water vapor in a column was condensed onto the surface. The RT code assumes that this water vapor is well-mixed up to its condensation level. Carbon monoxide amounts are input in a number mixing ratio, typically in units of parts per million (ppm). The RT code also assumes that this CO amount is well-mixed throughout the atmosphere along the incident and emergent rays.

3.3. Retrieval Method

[26] Once all LUTs have been created and filled in, the actual process of retrieving gas abundances from the CRISM observations can begin.

[27] The retrievals occur in a specific order, i.e., CO_2 must be retrieved first since it determines the surface pressure that is a necessary input for the other retrievals. However, with that exception, the procedure is essentially the same for all three gases.

[28] First, the geometry of the observation spectra must be determined. Parameters describing the Sun and observation orientation geometry are taken from the Planetary Data System archived metadata, specifically, the derived data record files [*Murchie et al.*, 2007].

[29] Next, the *I/F* value of the center channel defined for the gas absorption band (Table 1) is pulled from the CRISM observation data, specifically the targeted reduced data record files [*Murchie et al.*, 2007].

[30] A one-dimensional function is derived by interpolating the discrete LUT in each of the geometric dimensions, using the observation geometry values, and in one environmental (optical depth) dimension, using optical depth retrieved from concurrent Mars Odyssey THEMIS observations [*Smith*, 2009]), at each of albedo values defined for the albedo parameter dimension. That is,

$$\left(\frac{I}{F}\right)_i = f(A_i)\Big|_{\overline{\mu}_0, \overline{\mu}, \overline{\varphi}, \overline{\tau}}, \ i = 1, m, \tag{2}$$

where the overbar indicates that the observed values were used. *m* was 10 for the LUTs used in this work (see Table 2). This function is then interpolated with the observed *I/F* continuum value, $R_{continuum}$, to determine the albedo value, *A*, appropriate to this observation and band.

[31] Once the band albedo has been found, it is used as an input parameter in the gas abundance LUT retrieval. The process is similar to that for deriving the albedo value, except that now our result values are absorption band depth strengths, *S*, and the addition of both atmospheric environmental parameters and the previously derived albedo are necessary.

[32] The atmospheric environmental parameters are all taken from climatological averages, rather than derived directly from CRISM or other instruments on MRO and calculated as a function of season, latitude, and longitude. The optical depth, τ, climatology is taken from multiple years of Mars Odyssey THEMIS observations [*Smith*, 2009]. Atmospheric temperature profile (represented by a constant lapse rate defined by two points in the atmosphere, T_l and T_h, at 0.1 and 2 scale heights, respectively, with a possible additional constant isothermal profile at approximately 140 K if the lapse rate would predict temperatures lower than that) and surface temperature are taken from Mars Global Surveyor Thermal Emission Spectrometer (TES) climatology [*Smith*, 2004]. The small difference in local time between the TES and CRISM observations is not corrected, and represents only a very minor possible source of error.

[33] A one-dimensional function is again derived, this time as a function of gas abundance, by interpolating the LUT using the known parameter values. For this situation, we have

$$S_i = f(q_i)\Big|_{\overline{\mu}_0, \overline{\mu}, \overline{\varphi}, \overline{\tau}, \overline{T}_l, \overline{T}_h, \overline{T}_s, \overline{A}[, \overline{P}_S]}, \ i = 1, m, \tag{3}$$

where *q* is the abundance amount appropriate to the species of interest, and the overbars indicate the observed values used. The surface pressure parameter, P_S, is obviously left out of the observation value parameter list when doing the CO_2 retrieval, since in that retrieval it is represented by the *q* variable and being solved for in this case. P_S is used in the subsequent retrievals of H_2O and CO.

[34] The observed absorption band strength, S_O, is calculated from the observation spectra using equation (1). The band strength function from equation (3) is interpolated with S_O to determine the abundance value, *q*, appropriate to the observation and band. The abundance value, *q* is then recorded, typically along with all of the other input parameter values (including albedo) and band strengths used in deriving the result.

3.4. Data Quality Filtering

[35] The previous description presents the algorithm under normal circumstances. An initial step that is not intrinsically a part of the algorithm but is used to control the quality of the results is a filtering on whether to perform the retrieval at all based on data input quality.

[36] First, if the absorption band strength for any species, S_O, has a value > 1 or < 0, it is rejected as unphysical or overwhelmed by noise and the retrieval algorithm is skipped. Note that the absorption band for one species in a particular spectrum may be bad in this sense (a result of individual noisy pixels that are a tiny fraction of the data set) while another band may still be valid for retrieval. If this criterion were met, the retrieval value for the affected species was set to a "bad flag" value, typically a large negative number, to ensure that the retrieval value would be ignored in further processing (e.g., averaging or binning).
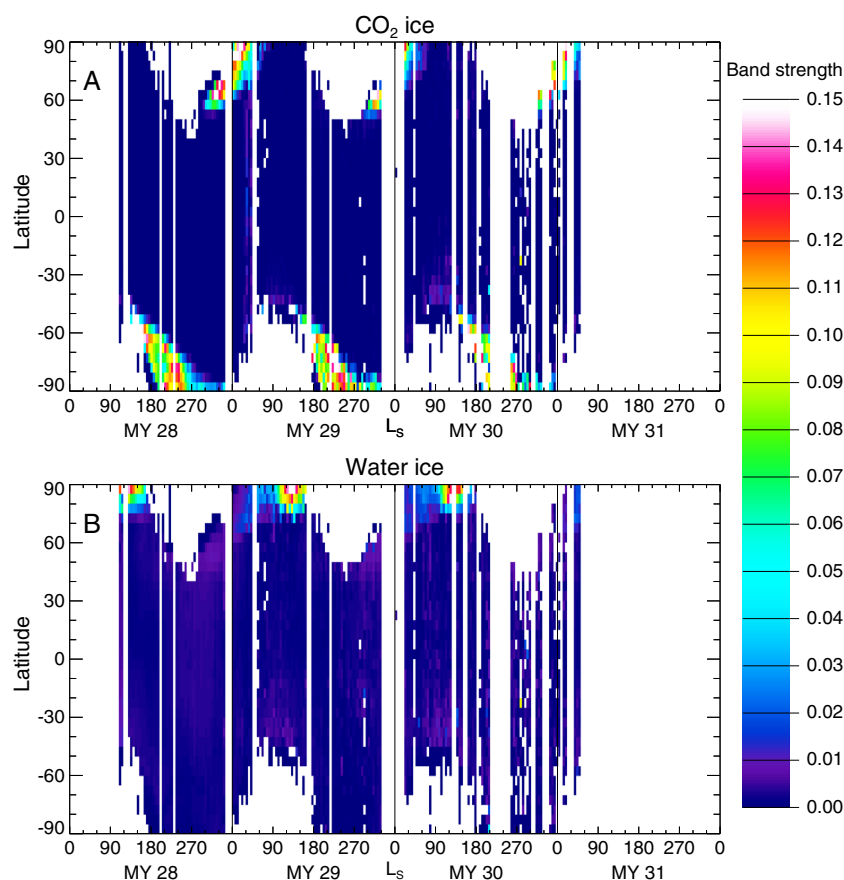
Figure 3. Zonally averaged (A) CO_2 and (B) H_2O ice (1.25 μm) absorption band index values as a function of latitude and season. A band index value of 0.1 was chosen as the cutoff for further use of a given spectra in retrieval analysis.

[37] Second, the gas bands considered here can potentially be contaminated by absorption from another species, in particular, surface ices. Figure 3 shows latitudinal and seasonal maps of the zonally averaged ice absorption feature strength, S_{ice} for CO_2 and H_2O ices. A value of 0.1 was chosen as a threshold value for both ice species based on correspondence of locations of this value with the visible location of the seasonal ice caps, and thus any spectra with an $S_{ice}(CO_2$ or $H_2O)$ > 0.1 was marked with a "ice contamination" flag to signal that it should be ignored during further processing of retrievals. The retrievals were still performed, but the values thus retrieved were flagged as being likely unreliable. 0.1 was chosen as the threshold since examination of band strength distribution showed that the value allowed avoidance of the major surface ice features which seriously contaminate the retrieval values, but still enabled retrievals at interesting polar locations where ice is potentially in exchange with the atmosphere but not appreciably influencing the retrieval amounts.

[38] In the figures and discussion in section 4 below, additional filtering of observations was also performed. Due to their generally higher noise, observations with high solar incidence angles (> 75°) and high CRISM IR detector temperatures (> 127.5 K) were rejected from inclusion in further analysis.

3.5. Validation and Uncertainties

[39] Although the LUT algorithm is faster, it is by nature less accurate than the full iterative radiative transfer calculations

that make up the RT algorithm in the precursor work of *Smith et al.* [2009]. A detailed discussion of the uncertainties in the RT method itself is presented in that paper as well. However, for this work, to determine just how much less accurate the LUT algorithm is compared to the RT algorithm, retrievals were done on all THOs, using both methods for comparison. The results, after filtering out "bad" data as described in the section 3.4, are shown in Figure 4.

[40] For the CO_2 and H_2O retrievals, the best fit line through the data differs from an exact one-to-one correspondence (the diagonal line in the figure) by less than 3%, less than our estimated error for these quantities and thus no "correction factor" was applied to correct values to those derived from the RT method. The best fit line for the CO retrievals are further from the one-to-one match. This appears to result from the choice of channel used for the band center. The best hyperspectral band center channels used in the RT method are not available in the multispectral subset used with both the THOs or MMOs in the LUT algorithm, but the retrieved values from the two methods linearly scale with each other, so a linear "correction factor" was applied to all of the CO results from the LUT algorithm to produce values in line with those from the RT method. All CO results presented in subsequent sections have this correction factor, 1.2543, applied to them.

[41] The spread about the one-to-one correspondence retrieval values line also gives an indication of the error in the LUT algorithm relative to the RT algorithm. For the CO_2
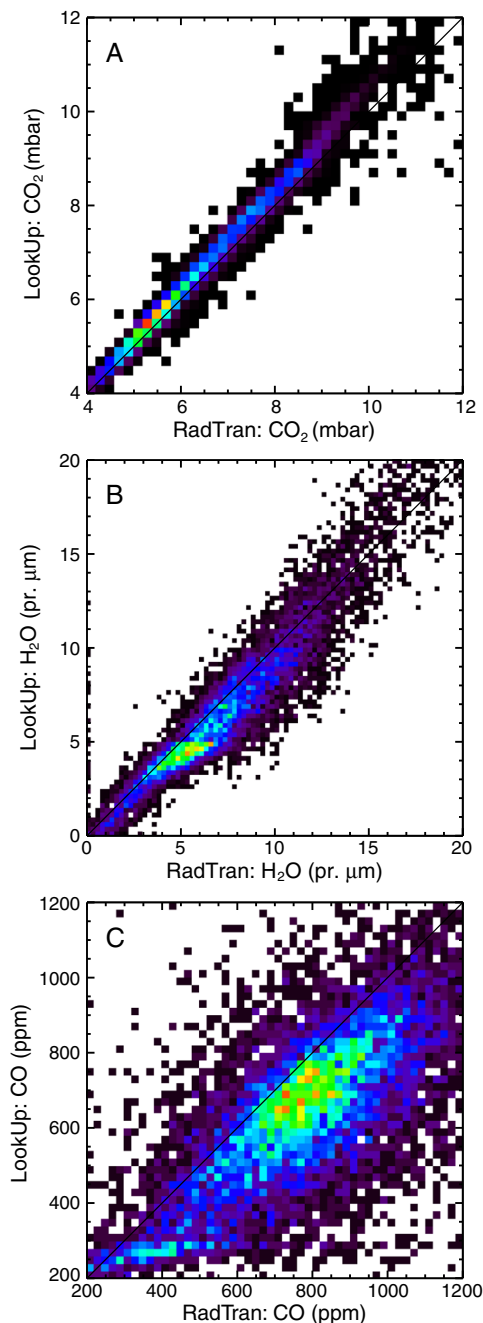
Figure 4. Binned density scatter plot of gas abundance retrieval values for (A) CO_2, (B) H_2O, and (C) CO, from the same THO observation, using the same central, 2 km square spatial region in each observation to produce an average spectra for retrieval. The range on the axes focuses on where the majority of data lies, rather than the full range realized. Observation count density plot scaling is arbitrary, but monotonic; red is many, (dark) purple is few, and white is none. The black diagonal lines represent a one-to-one correspondence between the two methods' retrieval values.

retrievals, the $1 - \sigma$ standard deviation error is 0.25 mbar. For H_2O, it is 3.25 precipitable microns. For CO, the weakest absorption band, it is 190 ppm. However, these errors are based on spatially averaged spectra, using on the order of 10,000 pixels, and thus an individual pixel's error may be

many times greater. During Mars Year 28 $L_s \approx 270°–310°$, there was a planet-encircling dust storm [*Smith*, 2009] and uncertainties may be somewhat higher during that time.

4. Results and Discussion

[42] The previously described LUT retrieval method was used to derive results in two modes, "averaging mode" and "pixel-by-pixel mode". The difference mainly relates to how an individual CRISM observation was handled.

[43] In "averaging mode", all the spectra in a region of about 2 km square were averaged together, and a single abundance value was reported back. For THOs, one square region was taken from the center of the observation. Centering in the cross-track direction is important as it minimizes the effect of the small shift in wavelength that occurs for a given CRISM channel in pixels along the cross-track sample direction. The change increases with distance from the center of the field of view, and is nonexistent or minimal for an area around the center. For MMOs, where typically the individual observation consists of a very long along-orbit-track length, multiple square regions per observation were used, with the region centered in the cross-track direction (to again minimize the channel wavelength drift), and then stacked one after the other in the along-track direction. In either observation type, the single abundance values per averaging region were collected in a large database for further processing.

[44] In "pixel-by-pixel mode", retrievals were performed on the spectrum in each individual pixel in an observation, either MMO or THO. This mode preserves the ability to detect patterns across an individual observation, but at the expense of reducing noise through averaging. A hybrid mode can be employed to address noise, where a sliding boxcar average of defined width can be used to average the spectra in I/F space before performing the retrievals and the average of the sliding boxcar region reported back for the central pixel.

[45] This section will describe the results from both modes, first for the "averaging mode," with which it is easier to compare to previous instruments, and then for the "pixel-by-pixel mode."

4.1. "Averaging" Mode

4.1.1. Carbon Dioxide

[46] The retrieval of CO_2 abundance from near-nadir CRISM observations is nearly equivalent to the measurement of surface pressure, because CO_2 constitutes the vast majority of the total atmospheric mass. CO_2 is also responsible for the strongest absorption features in the CRISM spectral range, and hence its retrieval tends to have the largest signal-to-noise of any of the gas retrievals. Figure 5 shows a map of the retrieved CO_2 column mass divided by an assumed constant CO_2 mixing ratio of 0.9532 [*Owen et al.*, 1977] to yield an equivalent surface pressure. The data included in the figure spans the period $L_s = 0°–30°$, and has been spatially averaged in bins of 5° size in latitude and longitude. Since the map shows relative spatial variations it is essentially also a retrieval of the global topography. Indeed, the retrieved surface pressure and the topography, derived from Mars Orbiter Laser Altimeter (MOLA) [*Smith et al.*, 2001] and overlain as contours in Figure 5, agree well as expected.
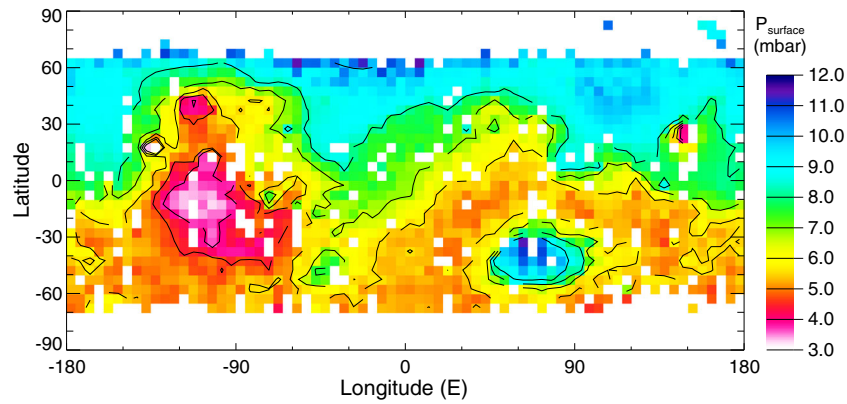
Figure 5. Map of surface pressure as determined from CO_2 retrievals. Data used is restricted to the period L_s=0°–30°, and has been averaged in 5° (in latitude and longitude) bins. Lines on top of the color map show contours of topography, every 2 km from –5 to 5 km.
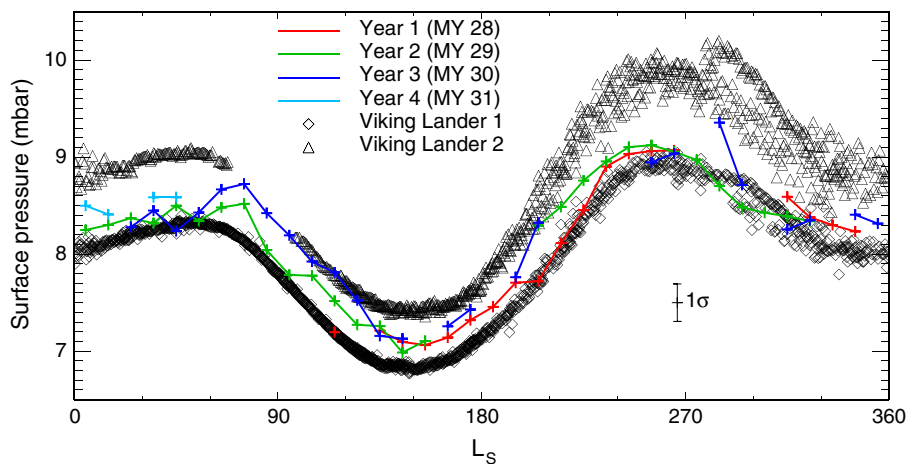
Figure 6. Plot of globally averaged surface pressure, color coded by Mars Year (MY), for all CRISM observations in the surface height range of 2–3 km. The mean standard deviation error bar is also shown below the plot; however this standard deviation is only representative of the spread of data values that went into calculating the mean, and not the error on each individual measurement. Symbols show daily-average surface pressure measurements from both Viking Lander missions (not separated by year) for comparison. Retrieval data has been scaled to adjust the mean surface height to one intermediate to the Viking Landers (approximately –3.5 km), and using the mean of the climatological air temperatures in the retrieval data, to ease the visual comparison.

[47] The CRISM surface pressure retrievals also allow the seasonal cycle of CO_2 to be illustrated. Figure 6 shows the globally averaged surface pressure as calculated from the retrievals, for all observations that fall in the topographic range of 2–3 km, and scaled to a height intermediate between that of the Viking Landers for easier visual comparison. Daily-average surface pressure measurements from both of the Viking Landers [*Tillman*, 1988] are also plotted. It should be noted that the curves from CRISM cannot be expected to lie directly over either VL record for (at least) two reasons. First, the CRISM observations were not sampled at the same location during the whole Martian year, and are an average over a set of observations whose locations change in each time binning interval. Second, due to Mars' hemispherical dichotomy, the restriction of data used to a specific surface height range tends to introduce a seasonal bias based on illumination conditions. The former should only affect differential

sampling of large-scale standing pressure systems, (e.g., the persistent high under the downwelling branch of the tropical mean overturning circulation), but the latter can also affect the inferred seasonal cycle. Taking those caveats into account, the CRISM observations agree well with the general cycle of pressure from the two landers, adding significantly to confidence in the retrieval. The high degree of interannual repeatability of the VL surface pressure records is a striking feature of the Martian climate system, but given the variance in the CRISM measurements and sampling, the question of whether the surface pressure cycle remains this tightly repeatable 30 Earth years later cannot be addressed.

[48] A powerful advantage of CRISM retrievals of surface pressure is the spatial sampling over a wide range of locations on the planet. The surface pressure at any location is complicated by factors such as topography and large-scale dynamical systems including the thermal tide, and other sources of bias

(see *Forget et al.* [2007] for examples and detailed analysis), and thus such a data set is ideally suited for use with, and analysis by, general circulation models (GCMs).

4.1.2. Water

[49] Water vapor retrievals are crucial to tracking the cycling of water between the surface and the atmosphere, and represent one of CRISM's main science objectives [*Murchie et al.*, 2007]. Whereas water vapor is of major interest for Mars climate science, water vapor retrievals have been difficult for instruments sent to Mars since the Viking Orbiters, with water vapor information generally being more sparse and of generally lower quality than that available for temperature, dust opacity and water ice opacity [*Smith*, 2004; *McCleese et al.*, 2007; *Smith et al.*, 2009; *Maltagliati et al.*, 2011]. Thus, information on water vapor from CRISM is of extremely high value.

[50] The global and seasonal behavior of water vapor as retrieved by CRISM is shown in Figure 7A. Longitudinally-averaged column water vapor retrieval amounts are plotted as a function of latitude and season for the over 3 Martian years of data thus far available. Data are binned by $5°$ of L_s and latitude. Familiar features of the water cycle as previously observed by the Viking Orbiter Mars Atmospheric Water Detector (MAWD) [*Jakosky and Farmer*, 1982] and Mars Global Surveyor/TES [*Smith*, 2004] can easily be seen. The dominant signal is the peak of vapor in northern summer, associated with the exposure of the northern residual water

ice cap. Water vapor amounts peak during this season across the northern hemisphere, peaking later in the season in any particular latitudinal band as latitude decreases equatorward. This shift in time of the seasonal peak may be a signature of transport or release of water from the regolith [*Jakosky*, 1983a, 1983b; *Richardson and Wilson*, 2002; *Montmessin et al.*, 2004; *Böttger et al.*, 2005]. The other major peak in water vapor amount occurs near the southern pole in southern late spring as the south seasonal cap sublimes. This appears to be the water sublimated from the seasonal water ice cap, whose extent (in both hemispheres) is shown in the simple mapping of water ice absorption strength in Figure 7B. A secondary peak in water vapor amount in the northern tropics at this season appears to be the signature of transport of water vapor sublimed from the southern seasonal cap into the northern hemisphere by the tropical mean overturning circulation ("Hadley cell") [*Richardson and Wilson*, 2002].

[51] Figure 7A also shows a very dry atmosphere starting around $L_s=270°$ in the first Martian year of CRISM and MRO operations [*Smith et al.*, 2009]. Similar dry periods in the southern hemisphere were observed by MAWD and TES and appear to be associated with very large dust storms (the 2007 global storm in the case of the first MRO year). Even though the increased air temperatures during the storms would produce a decrease in the relative humidity, it is not clear why they create a decrease in the total water column amount. A decrease in
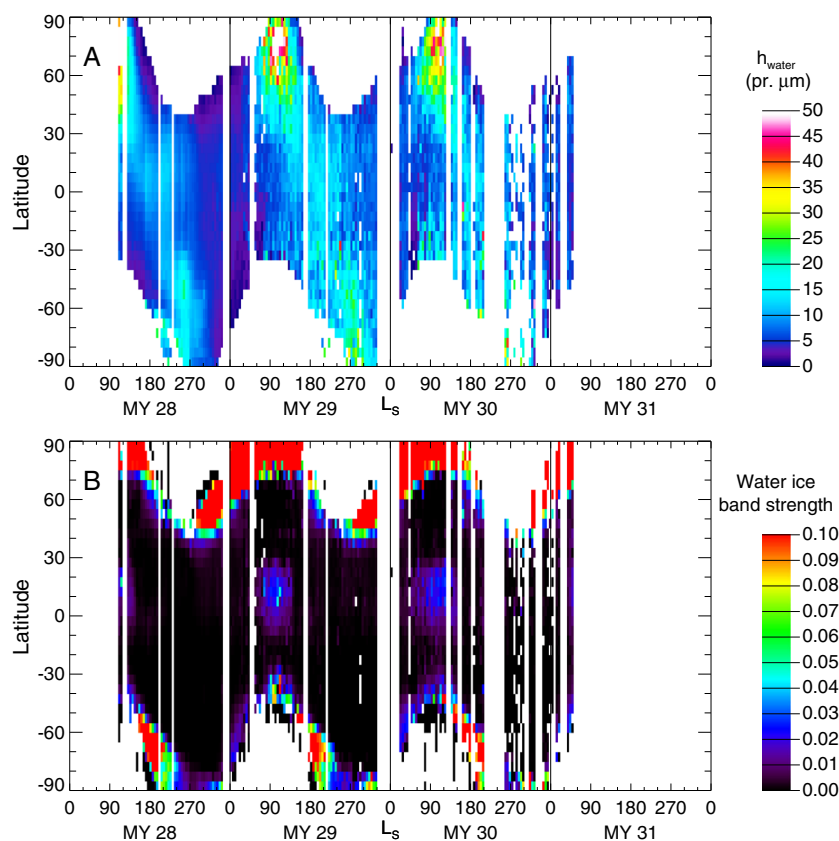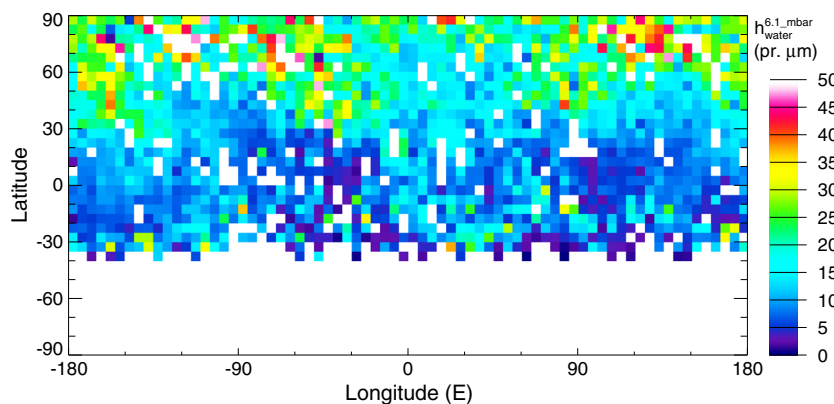

Figure 7. Zonally averaged (A) column water vapor retrieval amounts and (B) surface and atmospheric water ice (1.5 µm) absorption band strengths as a function of latitude and season. Data are binned by $5°$ in L_s and latitude. In (B), the increase in band strength in the northern tropics centered around $L_s=90°$ is indicative of the presence of ice in the aphelion tropical cloud belt, and is not surface ice.
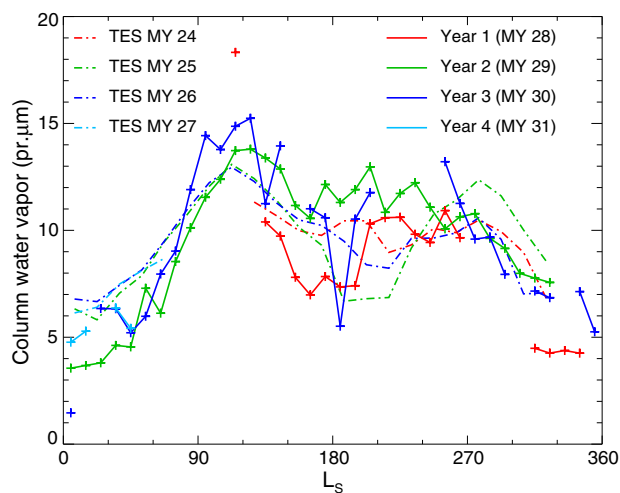
column integrated vapor amount is equivalent to a decrease in mass mixing ratio (under the well-mixed assumption), but the total atmospheric mass does not increase during a global dust storm. The mass of dust in the atmosphere during a major dust storm is comparable to the total mass of water vapor [*Martin*, 1995] and thus drying of the atmosphere by water vapor being absorbed by ambient dust aerosol particles does not appear likely. Although high optical depth during the large dust storm can prevent the entire atmospheric column from being sensed, and could therefore have lead to anomalously low retrieved water vapor abundance, this is also not likely the main cause for the observed low water vapor since the dry conditions lasted well beyond L_s=310°, when the dust storm had cleared and dust optical depths had returned to nominal, low values. Simulations from a GCM with an active (exchanging) regolith [*Böttger et al.*, 2004] suggest that the drying may be associated with surface cooling (due to shading of the surface by the optically thick dust storm clouds) which allows the regolith to adsorb more moisture from the atmosphere.

[52] The spatial distribution of water vapor around L_s=120° in early to middle northern summer is shown in Figure 8. The water amounts have been scaled to a common 6.1 mbar pressure surface to remove the effects of topography. Data used to build the map span a 30° window of L_s around the central time, and were averaged into 5° latitude and longitude bins. Although averaged for a very slightly longer period, this figure can be compared with the TES water vapor retrievals shown in Figure 17 of *Smith* [2004]. The TES data show a very distinct pattern that *Smith* [2004] show is generally correlated positively with albedo and negatively with thermal inertia, and is very consistent year to year. Thus, retrieved water abundances from all years for this seasonal interval have been averaged together in generating Figure 8. The resulting spatial pattern is similar to, but somewhat noisier than, the TES data. The spatial pattern may result from large-scale structure in the latitudinal vapor transport, or the correlations with albedo and thermal inertia potentially indicate thermal control over adsorptive exchange [*Böttger et al.*, 2005].

[53] Globally averaged water vapor retrieval amounts from both CRISM and TES as a function of season are shown in Figure 9 and separated by year. CRISM observational data
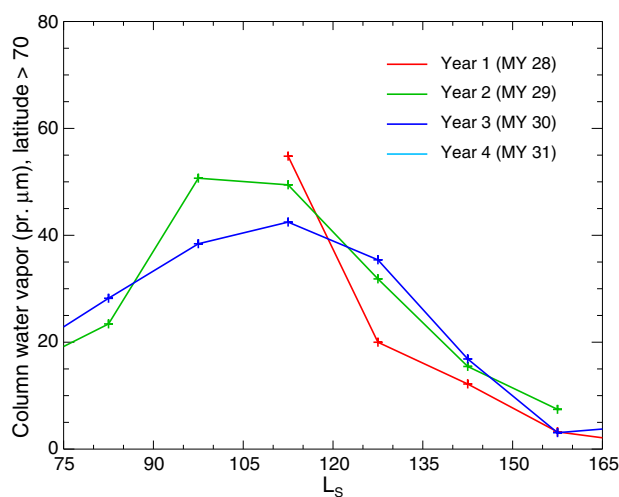
Figure 9. Plot of globally averaged column water vapor retrievals, color coded by Mars Year (MY) for all CRISM observations. Data are binned in time every 10° of L_s and in space by 5° of latitude and longitude. Global averages were calculated from area-weighted map-binned results for each temporal binning period. Some of the scatter in the plot, including some year-to-year differences, will be due to differing global coverage (e.g., see Figure 7 for latitudinal range of coverage) and spatial location of observations during any temporal binning period. In no temporal bin was the areal coverage more than about 40% of the total planetary surface area.

were collected into bins of every 10° of L_s. The general peak in global amounts during northern summer with a secondary peak during southern spring and early summer, as discussed above in reference to Figure 7A, can be seen. Errors in the column water vapor retrieval amounts from TES are approximately a few precipitable microns [*Smith*, 2004], while those from CRISM are a factor of two or more larger. Thus, confirmation or denial of the hypothesis of the existence of interannual variability (of less than the order of a few precipitable microns) in the global water cycle cannot be made with this data set.

[54] Regional average water vapor retrieval amounts in the north polar region during late spring and summer are shown

Figure 8. Map of column water vapor retrieval amounts around the L_s=120° season, scaled to a common pressure surface at 6.1 mbar. Data covers a 30° window around the central time, and has been averaged in 5° (in latitude and longitude) bins.

Figure 10. Plot of column water vapor retrievals, color coded by Mars Year (MY) averaged over the north polar region for all CRISM observations north of latitude 70°N. Data are binned in time every 15° of L_s, and any spectra showing ground ice have been rejected from the average.

in Figure 10. The data plotted here include all observations north of 70°N, but exclude any spectra showing surface ice contamination as discussed in section 3.4. The figure shows the increase and peak in water vapor after L_s=90° as the residual cap sublimes and then disappears around that time. Amounts drop off after L_s=120° as the polar region starts cooling again, and surface condensation begins slowly again. Column water vapor retrieval values in this region are consistent with similar polar values derived from TES [*Pankine et al.*, 2009] and a reanalysis of the MAWD data [*Fedorova et al.*, 2010].

4.1.3. Carbon Monoxide

[55] Carbon monoxide is responsible for the weakest of the three atmospheric absorption bands that we characterized, and so subject to the greatest amount of noise in the retrievals. However, in "averaging mode", the number of spectra used reduces the noise.

[56] Figure 11A displays the longitudinally-averaged CO retrieval amounts as a function of latitude and season. Data are binned by 5° in L_s and latitude. Low concentrations in the polar (especially south) regions can be detected, along with a generally larger equatorial concentration. Even the equatorial amounts show some seasonal dependence though, with the northern summer seasons seeing a relative maximum in concentration with the relative minimum occurring almost exactly one-half year later in southern summer.

[57] The photochemical lifetime of CO in the Martian atmosphere is of order a few years [*Clancy and Nair*, 1996]. As such, CO can be considered a noncondensable
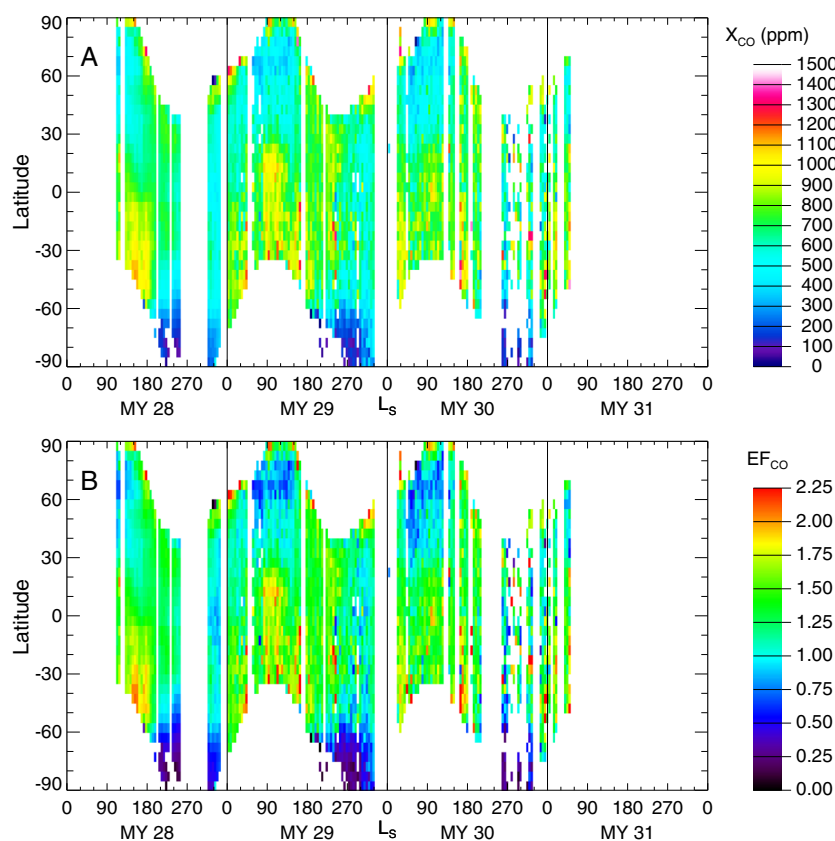
Figure 11. Zonally averaged (A) carbon monoxide retrieval amounts and (B) carbon monoxide "enhancement factor" (using the definition in Appendix A of *Lian et al.* [2012]) as a function of latitude and season. Data are binned by 5° in L_s and latitude. The gap after L_s=270° in the first year of observations is when the 2007 global dust storm occurred, and CO retrievals from this period were rejected due to unexpectedly large variance and unphysical amounts.

passive tracer, with measurements yielding information that is similar to measurements of argon obtained from Gamma Ray Spectrometer (GRS) observations [*Sprague et al.*, 2012]. The most significant feature in the GRS Ar data is the extreme level of Ar enhancement in southern winter, and which current Mars GCMs poorly match (discussed by *Lian et al.* [2012]). The GRS Ar retrievals, however, are noisy so the behavior (at much lower amounts) of Ar (or similar noncondensables like CO) away from the southern winter pole is less well illustrated. Conversely, the CRISM CO abundance retrievals cannot cover the peak enhancement during southern winter polar night due to the reliance on solar illumination. Yet when the pole is illuminated in southern summer, the CRISM CO abundance retrievals do yield information at a higher level of precision compared to GRS. Since both Ar and CO are effectively passive, their column integrated abundances can both be converted to an "enhancement factor" (EF), as described in Appendix A of *Lian et al.* [2012] and shown in Figure 11B.

[58] A striking feature of Figure 11B is the increase of EF that occurs in proximity to the southern seasonal cap during southern winter. This increase is due to the condensation of CO_2 onto the seasonal ice cap combined with modest leakage of noncondensables, including CO, out of the southern winter polar vortex. Around $L_s=180°$, EF decreases near the cap edge as sublimation over the whole area of the seasonal cap begins with the return of daylight to the center of the cap. The strong decrease of EF below unity, i.e., the dilution of noncondensables like CO by CO_2, is due to sublimation of CO_2 into an atmosphere that has partially mixed with the lower latitudes since that same CO_2 condensed onto the polar cap earlier in the year. The CO_2 fraction in this cap-edge region now exceeds the global average.

[59] Figure 12 shows CO abundances converted to EF and plotted in 15° latitude wide bands for ease of comparison with the GRS Ar data [*Sprague et al.*, 2007]. In the very high southern latitudes, the EF decreases to values as low as 0.1–0.3. Similarly low values are predicted by some (but not all) GCM simulations of condensable dilution [*Lian et al.*, 2012] and this CRISM CO data could be used in GCMs as a diagnostic at a level of accuracy that is greater than that of GRS Ar at this season. The tendency of the CO EF to show a small cyclic variation around a value of 1 at lower latitudes is theoretically expected, and provides confidence in the CO retrievals.

[60] The latitudinal and longitudinal distribution of CO amounts is shown in Figure 13. Data is taken from a 30° of L_s period around $L_s=240°$, and were averaged in 5° latitude and longitude bins. The previously mentioned gradient
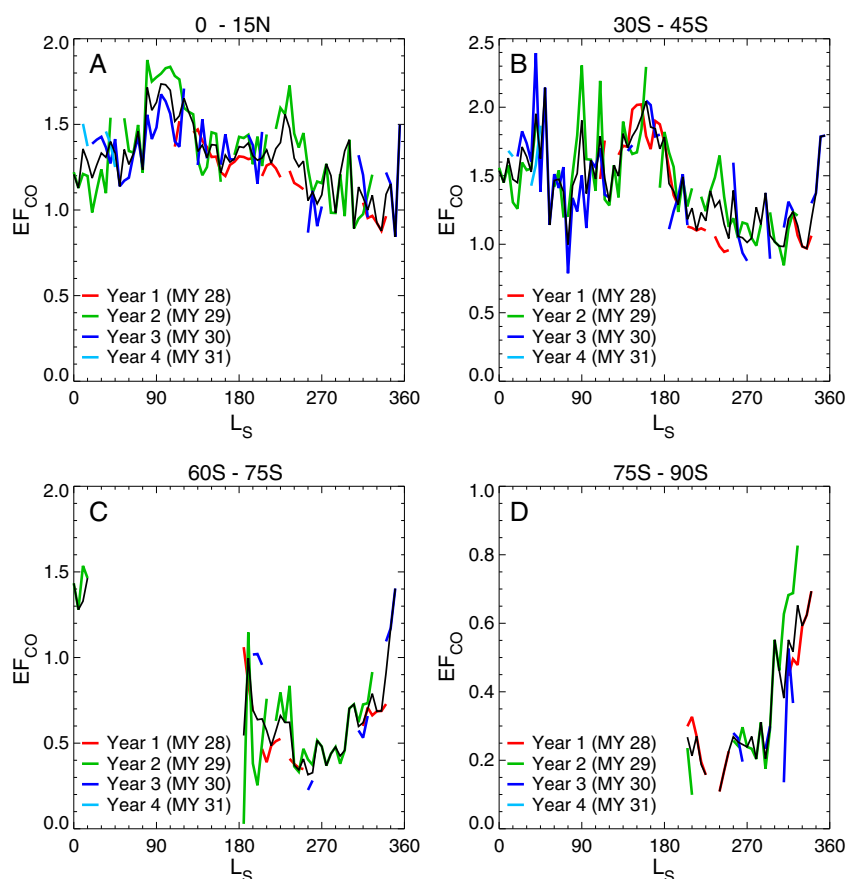
Figure 12. Area-averaged (360° of longitude and 15° of latitude) CO abundance retrievals converted to "enhancement factor" (using the definition in Appendix A of *Lian et al.* [2012]) as a function of season for 4 different latitude bands: (A) 0°N–15°N, (B) 30°S–45°S, (C) 60°S–75°S, and (D) 75°S–90°S. Values are color-coded by Mars Year (MY), and the black line is an average of all years for which there is data at that given time.
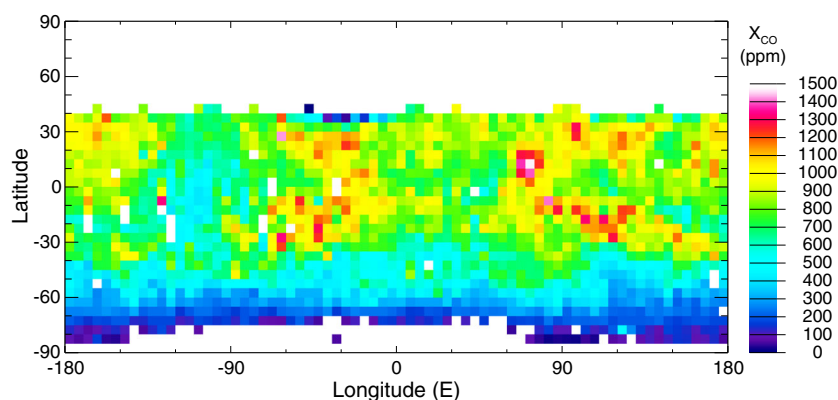
Figure 13. Map of carbon monoxide retrieval amounts around the L_s=240° (late southern spring) season. Data cover a 30° window around the central time, and has been averaged in 5° (in latitude and longitude) bins.

from large equatorial amounts to the very low, almost nonpresent, amounts around the south polar cap can be easily seen. There appears to be a weak correlation with topography around the Tharsis plateau and Valles Marineris canyon system, but not with the deep Hellas and Argyre basins, suggesting that the well-mixed assumption is mostly valid, but may need better observations to confirm it.

4.2. "Pixel-by-pixel" Mode

[61] The second innovation relative to the precursor work of *Smith et al.* [2009] is the ability to do retrievals on the spectra of individual pixels in a given CRISM observation. Although that capability exists with the RT algorithm used there, the computational overhead of that method makes retrieving values for an entire image similar in time to doing the retrievals over all THOs in averaging mode. With the LUT algorithm, the speed is orders of magnitude faster, and thus individual image retrievals can be presented here showing intraobservational variations, if any exist.

4.2.1. Valles Marineris

[62] One example of a "pixel-by-pixel" mode retrieval for an MMO observation is shown in Figure 14. It shows the results from the three gas retrievals of a portion of an extended MMO that crossed two of the canyons Valles Marineris. The upper row of plots show the surface pressure retrieval and the MOLA-derived topography, both as a cross-track average (Figure 14A) and for each individual pixel (Figures 14B and 14C). Surface pressure amounts can be seen to clearly and closely follow the topographic changes, as expected. The lower row of plots show the retrievals of column water vapor and CO mixing ratio, as a cross-track average (Figure 14D) and for each individual pixel (Figures 14E and 14F). Column water vapor also follows the changes in topography closely, as is expected for a well-mixed quantity. The CO retrievals represent a mixing ratio, and should be independent of both topography and surface pressure, although there appears to be a slight variation in line with topography changes.

4.2.2. Gale Crater

[63] Gale Crater is the landing site of the Mars Science Laboratory (MSL) and many CRISM observations were acquired in this region in support of landing site characterization. A pixel-by-pixel retrieval of gas abundances for any one of these CRISM observations for Gale Crater shows

essentially the same information as was displayed above for Valles Marineris: CO_2 retrievals closely follow topography, and CO and H_2O maps show instrumental noise structure rather than any physical structure in the observations. The lack of structure is not necessarily surprising as it confirms that processes on scales larger than a few tens to hundreds of kilometers are controlling the water vapor distribution, i.e., it is largely smoothed by atmospheric motions rather than being locally controlled by small scale sources and sinks. However, the frequent targeting of Gale and the pixel-by-pixel mode of retrieval do allow production of useful local data on the seasonal cycle of water vapor at Gale Crater. The differences in retrieval values across an individual observation can be used to define both a mean and variance of the observation retrieval for comparison.

[64] The seasonal cycle of column water vapor abundance at Gale Crater is shown in Figure 15. The variance of any single measurement is large, but the pattern of variation over the year is clear and consistent with understanding derived from the global mapping. Column water vapor amounts tend to be in the range of a few precipitable microns to somewhat over 10. The seasonal cycle is single-peaked at just after L_s=180° and with an extended minimum plateau from the start of southern summer until just before the start of northern summer. Situated near the equator, this timing of the maximum water vapor corresponds well with the phasing of the vapor "tongue" that is seen to extend southward from the northern polar cap [*Jakosky and Farmer*, 1982; *Smith*, 2004; *Smith et al.*, 2009]. Water vapor will be observed at the Gale Crater MSL landing site by the Rover Environmental Monitoring Station, and these CRISM observation retrievals should provide useful context for the MSL/Rover Environmental Monitoring Station observations.

5. Summary

[65] Gas abundance retrievals were made from CRISM spectral observation data over the approximately 3 Martian years of operation based on the radiative transfer code of *Smith et al.* [2009]. An efficient look-up table algorithm was constructed to perform these calculations quickly and accurately enough to allow retrievals of individual pixels in a given observation. The algorithm was designed to work with the two major types of CRISM observations, multispectral
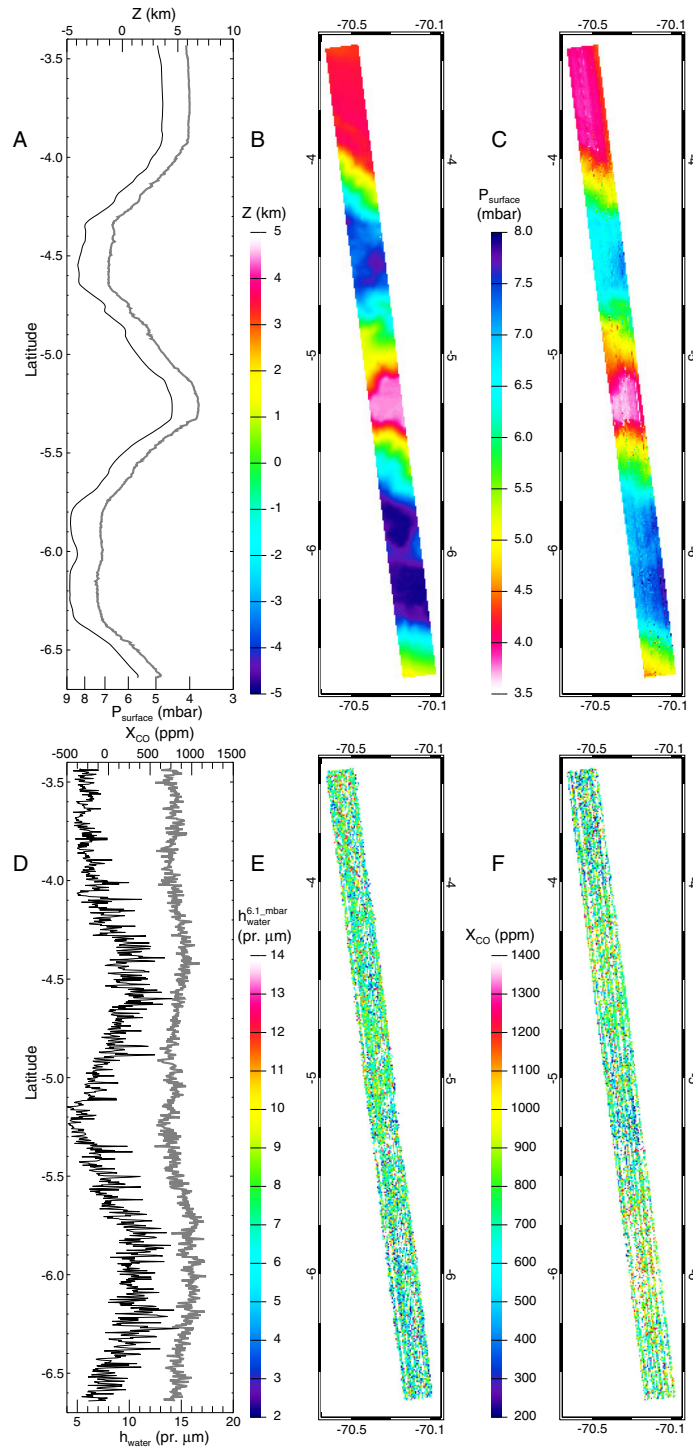
Figure 14. Retrieved gas abundances for each pixel for an example MMO observation, MSP000032FE_05. The region shown is from the southern half of this observation, and covers the period where the observation crosses two of the canyons of Valles Marineris. Line plots show cross-track averages to more easily visually compare quantities. (A) Line plots of surface height (black thin line, upper axis scaling) and retrieved surface pressure (gray thick line, lower axis scaling). The retrieved surface pressure very closely follows the changes in topography. (B) Color map of topography, as taken from the derived data record meta-data for the observation, and ultimately derived from MOLA topography. (C) Color map of retrieved surface pressure from the spectrum of every pixel. (D) Line plots of retrieved column water vapor amounts (black thin line, lower axis, values scaled to a reference surface pressure of 6.1 mbar), and retrieved carbon dioxide mixing ratios (gray thick line, upper axis). (E) Color map of retrieved column water vapor, scaled to a reference surface pressure of 6.1 mbar, from the spectrum of every pixel in the observation. (F) Color map of the retrieved CO mixing ratio from the spectrum of every pixel in the observation.
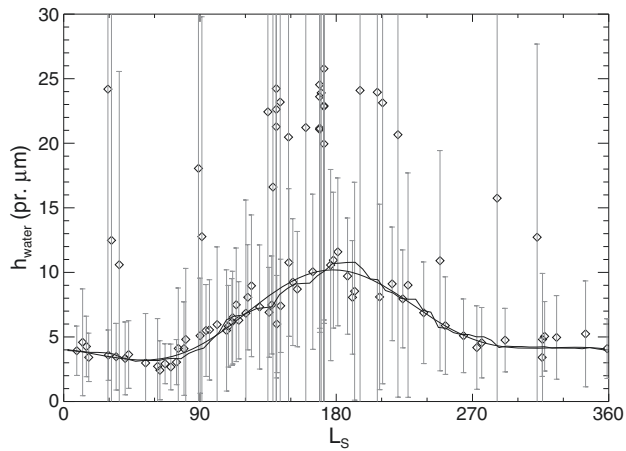
Figure 15. Variation of column water vapor abundance in the Gale crater region as derived from CRISM retrievals. Approximately 100 observations spread out over 4 years of the mission are represented, but owing to the general repeatability of the global water cycle, are all treated as part of the same seasonal cycle. Black diamonds show the mean value over the whole observation, and the gray error bars are the variance of the individual pixel retrievals with respect to the mean of the observation. Mean values were adjusted for topographic (and seasonal surface pressure) variations in the image by scaling all values to a constant pressure of 6.1 mbar, and also recording the mean surface pressure in the image. Annual average surface pressure for the region was calculated by averaging all observations, and the individual observation means were rescaled from the 6.1 mbar reference surface back to this annual mean surface pressure, which was 6.85 mbar. The jagged black line is an error-weighted running boxcar average of width 60° of L_s. The smooth black line is a fit to this running average using Fourier analysis, but only keeping the annual and semi-annual components. The resulting equation that describes this fit to the seasonal cycle, on a constant pressure surface of 6.85 mbar, is: h_{water} (precipitable microns) $= 5.86 + 3.08 \sin(L_s - 94.52°) + 1.29 \sin(2L_s + 102.20°)$.

mapping observations and gimballed targeted hyperspectral observations.

[66] The major conclusions from the analysis of the results are:

1. Carbon dioxide retrievals are essentially retrievals of surface pressure. Surface pressure results match closely with previous spacecraft data, e.g., Viking Lander data.
2. Surface pressure results can be retrieved on a global scale, something that is not possible with lander data. Global-scale results can be used in further analysis and constraint in atmospheric models.
3. Column water vapor abundance retrievals, represented as time-averaged maps, global-average amounts, or north polar regional averages, match well with previous TES and MAWD results.
4. Carbon monoxide mixing ratio retrievals show the effect of the gas acting as a long lifetime, "noncondensable" species. If the gas abundance is represented by an "enhancement factor" and compared with retrievals of

other noncondensable species which also use such a representation, such as argon, the values and seasonal behavior compare quite well with other instruments' retrieval values.
5. Mapped retrievals of a whole CRISM observation show expected behavior. Carbon dioxide retrievals follow topography closely, and the column water vapor amounts also change in line with the topography and surface pressure as expected. Carbon monoxide retrievals show a mostly constant mixing ratio with the main variations being due to instrumental noise.
6. Using whole observation "pixel-by-pixel" retrievals to derive a mean and variance, the seasonal cycle of column water vapor abundance in the Gale Crater region of the MSL landing site has been presented for context for MSL observations.

References

Böttger, H. M., S. R. Lewis, P. L. Read, and F. Forget (2004), The effect of a global dust storm on simulations of the Martian water cycle, *Geophys. Res. Lett.*, *31*, L22702, doi:10.1029/2004GL021137.

Böttger, H. M., S. R. Lewis, P. L. Read, and F. Forget (2005), The effects of the martian regolith on GCM water cycle simulations, *Icarus*, *177*, 174–189, doi:10.1016/j.icarus.2005.02.024.

Clancy, R. T., and H. Nair (1996), Annual (perihelion-aphelion) cycles in the photochemical behavior of the global Mars atmosphere, *J. Geophys. Res.*, *101*(E5), 12,785–12,790, doi:10.1029/96JE00836.

Clancy, R. T., B. J. Sandor, M. J. Wolff, M. D. Smith, F. Lefèvre, J.-B. Madeleine, F. Forget, S. L. Murchie, F. P. Seelos, K. D. Seelos, H. A. Nair, A. D. Toigo, D. Humm, D. M. Kass, A. Kleinböhl, and N. Heavens (2012), Extensive MRO CRISM Observations of 1.27 μm O_2 Airglow in Mars Polar Night and Their Comparison to MRO MCS Temperature Profiles and LMD GCM Simulations, *J. Geophys. Res.*, *117*, doi:10.1029/2011JE004018.

Fedorova, A. A., S. Trokhimovsky, O. Korablev, and F. Montmessin (2010), Viking observation of water vapor on Mars: Revision from up-to-date spectroscopy and atmospheric models, *Icarus*, *208*, 156–164, doi:10.1016/j.icarus.2010.01.018.

Forget, F., A. Spiga, B. Dolla, S. Vinatier, R. Melchiorri, P. Drossart, A. Gendrin, J.-P. Bibring, Y. Langevin, and B. Gondet (2007), Remote sensing of surface pressure on Mars with the Mars Express/OMEGA spectrometer: 1. retrieval method, *J. Geophys. Res.*, *112*(E11), E08S15, doi:10.1029/2006JE002871.

Jakosky, B. M. (1983a), The role of seasonal reservoirs in the Mars water cycle: I. seasonal exchange of water with the regolith, *Icarus*, *55*(1), 1–18, doi:10.1016/0019-1035(83)90046-5.

Jakosky, B. M. (1983b), The role of seasonal reservoirs in the Mars water cycle: Ii. coupled models of the regolith, the polar caps, and atmospheric transport, *Icarus*, *55*(1), 19–39.

Jakosky, B. M., and C. B. Farmer (1982), The seasonal and global behavior of water vapor in the Mars atmosphere: Complete global results of the Viking atmospheric water detector experiment, *J. Geophys. Res.*, *87*, 2999–3019, doi:10.1029/JB087iB04p02999.

Lian, Y., M. I. Richardson, C. E. Newman, C. Lee, A. D. Toigo, M. A. Mischna, and J. M. Campin (2012), The Ashima/MIT Mars GCM and argon in the Martian atmosphere, *Icarus*, *218*, 1043–1070, doi:10.1016/j.icarus.2012.02.012.

Maltagliati, L., D. V. Titov, T. Encrenaz, R. Melchiorri, F. Forget, H. U. Keller, and J.-P. Bibring, (2011), Annual survey of water vapor behavior from the OMEGA mapping spectrometer onboard Mars Express, *Icarus*, *213*, 480–495, doi:10.1016/j.icarus.2011.03.030.

Martin, T. Z. (1995), Mass of dust in the Martian atmosphere, *J. Geophys. Res.*, *100*(E4), 7509–7512, doi:10.1029/95JE00414.

McCleese, D. J., J. T. Schofield, F. W. Taylor, S. B. Calcutt, M. C. Foote, D. M. Kass, C. B. Leovy, D. A. Paige, P. L. Read, and R. W. Zurek (2007), Mars Climate Sounder: An investigation of thermal and water vapor structure, dust and condensate distributions in the atmosphere,

and energy balance of the polar regions, *J. Geophys. Res.*, *112*(E11), E05S06, doi:10.1029/2006JE002790.

Montmessin, F., F. Forget, P. Rannou, M. Cabane, and R. M. Haberle (2004), The origin and role of water ice clouds in the Martian water cycle as inferred from a general circulation model, *J. Geophys. Res.*, *109*(E18), E10004, doi:10.1029/2004JE002284.

Murchie, S., R. Arvidson, P. Bedini, K. Beisser, J.-P. Bibring, J. Bishop, J. Boldt, P. Cavender, T. Choo, R. T. Clancy, E. H. Darlington, D. D. Marais, R. Espiritu, D. Fort, R. Green, E. Guinness, J. Hayes, C. Hash, K. Heffernan, J. Hemmler, G. Heyler, D. Humm, J. Hutcheson, N. Izenberg, R. Lee, J. Lees, D. Lohr, E. Malaret, T. Martin, J. A. McGovern, P. McGuire, R. Morris, J. Mustard, S. Pelkey, E. Rhodes, M. Robinson, T. Roush, E. Schaefer, G. Seagrave, F. Seelos, P. Silverglate, S. Slavney, M. Smith, W.-J. Shyong, K. Strohbehn, H. Taylor, P. Thompson, B. Tossman, M. Wirzburger, and M. Wolff (2007), Compact Reconnaissance Imaging Spectrometer for Mars (CRISM) on Mars Reconnaissance Orbiter (MRO), *J. Geophys. Res.*, *112*(E11), E05S03, doi:10.1029/2006JE002682.

Murchie, S. L., F. P. Seelos, C. D. Hash, D. C. Humm, E. Malaret, J. A. McGovern, T. H. Choo, K. D. Seelos, D. L. Buczkowski, M. F. Morgan, O. S. Barnouin-Jha, H. Nair, H. W. Taylor, G. W. Patterson, C. A. Harvel, J. F. Mustard, R. E. Arvidson, P. McGuire, M. D. Smith, M. J. Wolff, T. N. Titus, J.-P. Bibring, and F. Poulet (2009), Compact Reconnaissance Imaging Spectrometer for Mars investigation and data set from the Mars Reconnaissance Orbiter's primary science phase, *J. Geophys. Res.*, *114*, E00D007, doi:10.1029/2009JE003344.

Owen, T., K. Biemann, J. E. Biller, A. L. Lafleur, D. R. Rushneck, and D. W. Howarth (1977), The composition of the atmosphere at the surface of Mars, *J. Geophys. Res.*, *82*, 4635–4639, doi:10.1029/JS082i028p04635.

Pankine, A. A., L. K. Tamppari, and M. D. Smith (2009), Water vapor variability in the north polar region of Mars from Viking MAWD and MGS TES datasets, *Icarus*, *204*, 87–102, doi:10.1016/j.icarus.2009.06.009.

Richardson, M. I., and R. J. Wilson (2002), Investigation of the nature and stability of the Martian seasonal water cycle with a general circulation model, *J. Geophys. Res.*, *107*(E5), 5031, doi:10.1029/2001JE001536.

Smith, D. E., M. T. Zuber, H. V. Frey, J. B. Garvin, J. W. Head, D. O. Muhleman, G. H. Pettengill, R. J. Phillips, S. C. Solomon, H. J. Zwally, W. B. Banerdt, T. C. Duxbury, M. P. Golombek, F. G. Lemoine, G. A. Neumann,

D. D. Rowlands, O. Aharonson, P. G. Ford, A. B. Ivanov, C. L. Johnson, P. J. McGovern, J. B. Abshire, R. S. Afzal, and X. Sun (2001), Mars Orbiter Laser Altimeter: Experiment summary after the first year of global mapping of Mars, *J. Geophys. Res.*, *106*(E10), 23,689–23,722, doi:10.1029/2000JE001364.

Smith, M. D. (2004), Interannual variability in TES atmospheric observations of Mars during 1999-2003, *Icarus*, *167*, 148–165, doi:10.1016/j.icarus.2003.09.010.

Smith, M. D. (2009), THEMIS observations of Mars aerosol optical depth from 2002–2008, *Icarus*, *202*(2), 444–452, doi:10.1016/j.icarus.2009.03.027.

Smith, M. D., M. J. Wolff, R. T. Clancy, and S. L. Murchie (2009), Compact Reconnaissance Imaging Spectrometer observations of water vapor and carbon monoxide, *J. Geophys. Res.*, *114*(E13), E00D03, doi:10.1029/2008JE003288.

Smith, M. D., M. J. Wolff, R. T. Clancy, A. Kleinböhl, and S. L. Murchie (2012), Vertical Distribution of Dust and Water Ice Aerosol from CRISM Limb-Geometry Observations, *J. Geophys. Res.*, *118*, doi:10.1002/jgre.20047.

Sprague, A. L., W. V. Boynton, K. E. Kerry, D. M. Janes, N. J. Kelly, M. K. Crombie, S. Melli, J. R. Murphy, R. C. Reedy, and A. E. Metzger (2007), Mars' atmospheric argon: Tracer for understanding Martian atmospheric circulation and dynamics, *J. Geophys. Res.*, *112*(E11), doi:10.1029/2005JE002597.

Sprague, A. L., W. V. Boynton, F. Forget, Y. Lian, M. Richardson, R. Starr, A. E. Metzger, D. Hamara, and T. Economou (2012), Interannual similarity and variation in seasonal circulation of Mars' atmospheric Ar as seen by the Gamma Ray Spectrometer on Mars Odyssey, *J. Geophys. Res.*, *117*(E16), E04005, doi:10.1029/2011JE003873.

Tillman, J. E. (1988), Mars global atmospheric oscillations: Annually synchronized, transient normal mode osciallations and the triggering of global dust storms, *J. Geophys. Res.*, *93*, 9433–9451, doi:10.1029/JD093iD08p09433.

Wolff, M. J., M. D. Smith, R. T. Clancy, R. Arvidson, M. Kahre, F. Seelos, S. Murchie, and H. Savijärvi (2009), Wavelength dependence of dust aerosol single scattering albedo as observed by the Compact Reconnaissance Imaging Spectrometer, *J. Geophys. Res.*, *114*(E13), E00D04, doi:10.1029/2009JE003350.

Zurek, R. W., and S. E. Smrekar (2007), An overview of the Mars Reconnaissance Orbiter (MRO) science mission, *J. Geophys. Res.*, *112*(E11), E05S01, doi:10.1029/2006JE002701.